Bio-Design and Manufacturing (2025) 8:759–775
https://doi.org/10.1631/bdm.2400470

RESEARCH ARTICLE

Targeting cyclooxygenase-2 using photothermal-anti-inflammatory nanoparticles to inhibit tumor growth and metastasis

Jiahui Cai[1,2,3] · Zutong Cui[1,2,3] · Wenming Liang[1,2,3] · Jianming Sun[1,2,3] · Zihan Zhang[1,2,3] · Shasha Zhao[1,2,3] · Zhiwei Liu[1,2,3] · Xiaoling Li[1,2,3] · Jian Li[1,2,3]

Received: 21 November 2024 / Accepted: 5 March 2025

Abstract

Photothermal therapy (PTT) is a non-invasive and highly selective tumor treatment. However, it triggers an inflammatory reaction and other adverse effects, including damage to the surrounding healthy tissue and an increased risk of tumor proliferation and metastasis. The cyclooxygenase-2 (COX-2)/prostaglandin E2 (PGE2) pathway plays a crucial role in regulating tumor development. In this study, we revealed that PTT activates the COX-2/PGE2 pathway. To mitigate the PTT-induced inflammation, based on polydopamine (PDA) and HS-β-cyclodextrin (HS-β-CD), we constructed a photothermal/anti-inflammatory nanoparticle system (named ICG@PDA-β-CD/CEL) loaded with the anti-inflammatory drug celecoxib (CEL) and the photosensitizer indocyanine green (ICG), which targets COX-2. This system helps PTT by (1) reducing pro-inflammatory molecules such as PGE2, tumor necrosis factor-α, and interleukin-6 and inhibiting the COX-2 and nuclear factor kappa-B signaling pathways, (2) suppressing vascular endothelial growth factor production to inhibit tumor angiogenesis, and (3) preventing tumor cell migration and invasion. Further results indicated that ICG@PDA-β-CD/CEL significantly curtailed tumor cell invasion and migration in vitro and suppressed the COX-2/PGE2 pathway in vivo, thereby markedly inhibiting both orthotopic tumor growth and metastasis. ICG@PDA-β-CD/CEL exhibits potent antitumor effects through its combined anti-inflammatory and photothermal therapies, providing a promising strategy for alleviating PTT-related adverse effects.

✉ Jian Li
Lijianbio@ysu.edu.cn

[1] Nano-biotechnology Key Laboratory of Hebei Province, Yanshan University, Qinhuangdao 066000, China

[2] Hebei Key Laboratory of Applied Chemistry, Yanshan University, Qinhuangdao 066000, China

[3] School of Environmental and Chemical Engineering, Yanshan University, Qinhuangdao 066000, China

Graphical abstract

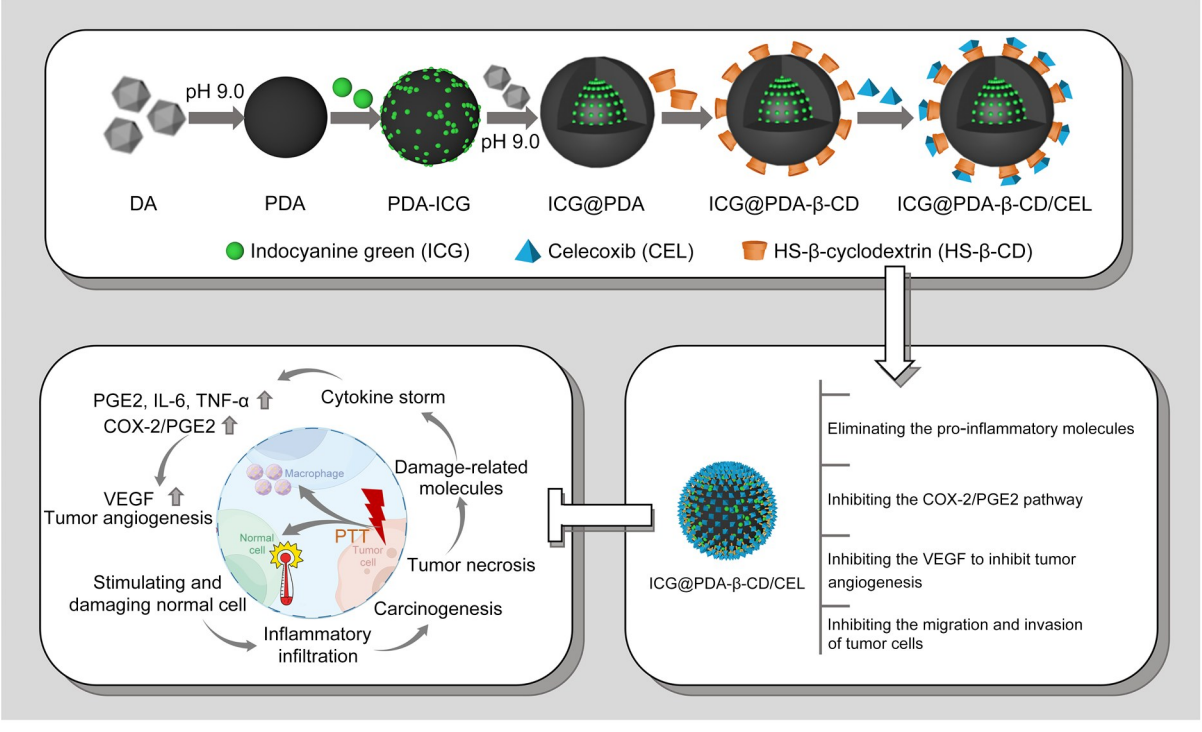

Keywords Photothermal therapy · Cyclooxygenase-2 (COX-2)/prostaglandin E2 (PGE2) pathway · Targeting COX-2 · Anti-inflammatory

1 Introduction

Photothermal therapy (PTT) uses cellular sensitivity to high temperatures to induce tumor cell apoptosis and is favored for its efficiency, noninvasiveness, and specificity [1]. However, PTT alone is frequently associated with severe side effects. During PTT, most tumor cells undergo necroptosis caused by excessive local temperatures. The molecules released by necrotic cells act as endogenous danger signals, which worsen inflammatory responses, induce cytokine storms, and promote tumor metastasis [2, 3].

Previous reports have determined cyclooxygenase-2 (COX-2) as a significant inflammatory mediator in tumor progression. COX-2, a key enzyme in synthesizing tumor cell-derived prostaglandin E2 (PGE2), is regulated by its downstream product PGE2 [4, 5]. PGE2, a potent carcinogen, promotes tumor development through several pathways [6]. PGE2 promotes angiogenesis via vascular endothelial growth factor (VEGF) [7], suppresses T and B cell proliferation [8], and activates inflammatory pathways, thereby supporting tumor growth, immune evasion, and chronic inflammation-related carcinogenesis. Consequently, understanding how to mitigate the acute inflammatory response, clear inflammatory molecules, and inhibit the COX-2/PGE2 pathway to alleviate the harsh effects of photothermal treatment and improve therapeutic outcomes remains a crucial focus.

COX-2 inhibitors are promising adjuvants to improve PTT against tumors [9]. Predominantly used COX-2 inhibitors include nonsteroidal anti-inflammatory drugs (NSAIDs) such as indomethacin, celecoxib (CEL), and nimesulide, which provide anti-inflammatory and analgesic effects [10, 11]. The combination of NSAIDs with photosensitizers presents an effective treatment modality that achieves efficient tumor suppression while minimizing adverse reactions. Several researchers have proposed similar strategies that have demonstrated some degree of tumor inhibition. Table S1 (supplementary information) summarizes and organizes these notable studies [9, 12–18]. Based on these results, we developed phototherapy-anti-inflammatory nanoparticles that target COX-2.

In our study, CEL was selected as the COX-2 inhibitor to target tumor cells and reduce inflammation. CEL serves as an effective agent for COX-2 targeting, which potentially

inhibits cancer cell growth and metastasis. Furthermore, indocyanine green (ICG) is a near-infrared (NIR) dye approved by the Food and Drug Administration. It produces photothermal and photodynamic effects under NIR excitation and is widely used in tumor therapy research [19, 20]. Therefore, ICG was selected as the photosensitizer and β-cyclodextrin modified polydopamine (PDA-β-CD) as the amphiphilic carrier [21]. The hydrophilic ICG was encapsulated within the inner layers of the PDA structure, whereas the hydrophobic CEL was embedded within the hydrophobic cavity of β-CD. This design resulted in the development of a photothermal-anti-inflammatory synergistic nanodrug delivery system, ICG@PDA-β-CD/CEL, which targets COX-2 and effectively fights against malignant tumors.

Once in the bloodstream, ICG@PDA-β-CD/CEL nanoparticles target COX-2-expressing tumor cells and accumulate within tumor tissues through the enhanced permeability and retention (EPR) effect. PDA and ICG work together to exhibit a dual photothermal effect that destroys the tumor cells. As a COX-2 inhibitor, CEL effectively suppresses inflammation and specifically targets the COX-2/PGE2 pathway, thereby mitigating related inflammatory factors and inhibiting peritumoral neovascularization. The result is an ideal tumor suppression effect through combined anti-inflammatory and PTT (Scheme 1).

Our study revealed that ICG@PDA-β-CD/CEL nanoparticles demonstrate excellent biosafety and significantly inhibit HeLa cell cloning, invasion, and migration in vitro. In U14 tumor-bearing mice, ICG@PDA-β-CD/CEL demonstrated higher tumor suppression rates in primary and metastatic tumors compared to ICG@PDA-β-CD alone. The CEL component effectively inhibited the COX-2/PGE2 pathway, not only reducing the spread of inflammatory signals and dampening the inflammatory response but also curtailing VEGF-mediated proliferation and vascular endothelial cell migration, thereby reducing angiogenesis and further preventing tumor growth and metastasis. The development of ICG@PDA-β-CD/CEL provides a viable strategy for managing PTT-induced adverse inflammatory reactions.

2 Materials and methods

2.1 Experimental materials

Sigma-Aldrich (USA) supplied dopamine hydrochloride (DA-HCl). Shanghai Bidepharm Technology Co., Ltd. (China) provided HS-β-cyclodextrin (HS-β-CD). Sinopharm Chemical Reagents Co., Ltd. (Shanghai, China) supplied ICG and CEL. Beyotime Biotechnology Co., Ltd. (Shanghai, China) provided the cell experiment kits used. Nanjing Jiancheng Biological Engineering (China) supplied assay kits for liver and kidney indicators (alanine aminotransferase (ALT), aspartate aminotransferase (AST), blood urea nitrogen (BUN), and creatinine (CRE)). Shanghai Enzyme-Linked Immunity Company (China) provided COX-2, PGE2, interleukin 6 (IL-6), tumor necrosis factor-α (TNF-α), and IL-10 enzyme-linked immunosorbent assay (ELISA) kits. All chemical agents utilized were of analytical grade.

2.2 Cell lines and animals

Procell Life Science & Technology Co., Ltd. (Wuhan, China) provided HeLa cells and U14 cells, which were cultured in Dulbecco's modified Eagle's medium containing 10% fetal bovine serum and 1% penicillin–streptomycin. The cells were cultured in a constant temperature incubator (Thermo Scientific, Waltham, MA) at 37 °C with 5% CO_2.

Beijing Charles River Laboratory Animal Technology Co. (China) provided 4–6 week-old female Kunming mice ((20±2) g, specific pathogen-free (SPF) grade, certificate number: SCXK (Beijing) 2016-0011) for animal experiments. The mice were randomly grouped after being injected with U14 cells to develop tumor models and were kept under standard conditions.

2.3 Synthesis of ICG@PDA-β-CD/CEL

2.3.1 Synthesis of PDA and ICG on PDA

A Tris-HCl buffer solution (pH: 9, 0.05 mol/L, 48 mL) was prepared, and 30 mg of DA-HCl was added and evenly dispersed under magnetic stirring at 150 r/min. Subsequently, 12 mL of isopropanol was added to initiate polymerization for 8 h. The resulting product was centrifuged at 14,000 r/min for 10 min and washed three times to obtain a small-sized PDA. ICG of 10 mg was then added to the PDA and co-incubated for 12 h. The PDA produces π–π interaction forces with molecules containing a π system, thereby adsorbing small molecules, such as ICG [22], forming the PDA-ICG product. The supernatant from the first centrifugation was collected, and its absorbance was measured to calculate the encapsulation rate (r_E) and drug loading (r_{DL}) of ICG according to Eqs. (1) and (2), respectively [23]. To prevent ICG detachment, the PDA-ICG was redissolved in Tris-HCl buffer solution, and 20 mg of DA-HCl was added to coat the surface of the PDA-ICG with an additional PDA layer, forming an "Oreo" structure, denoted as PDA-ICG@PDA (abbreviated as ICG@PDA).

$$r_E = \frac{W_i - W_r}{W_i} \times 100\%, \quad (1)$$

$$r_{DL} = \frac{W_i - W_r}{W_t} \times 100\%. \quad (2)$$

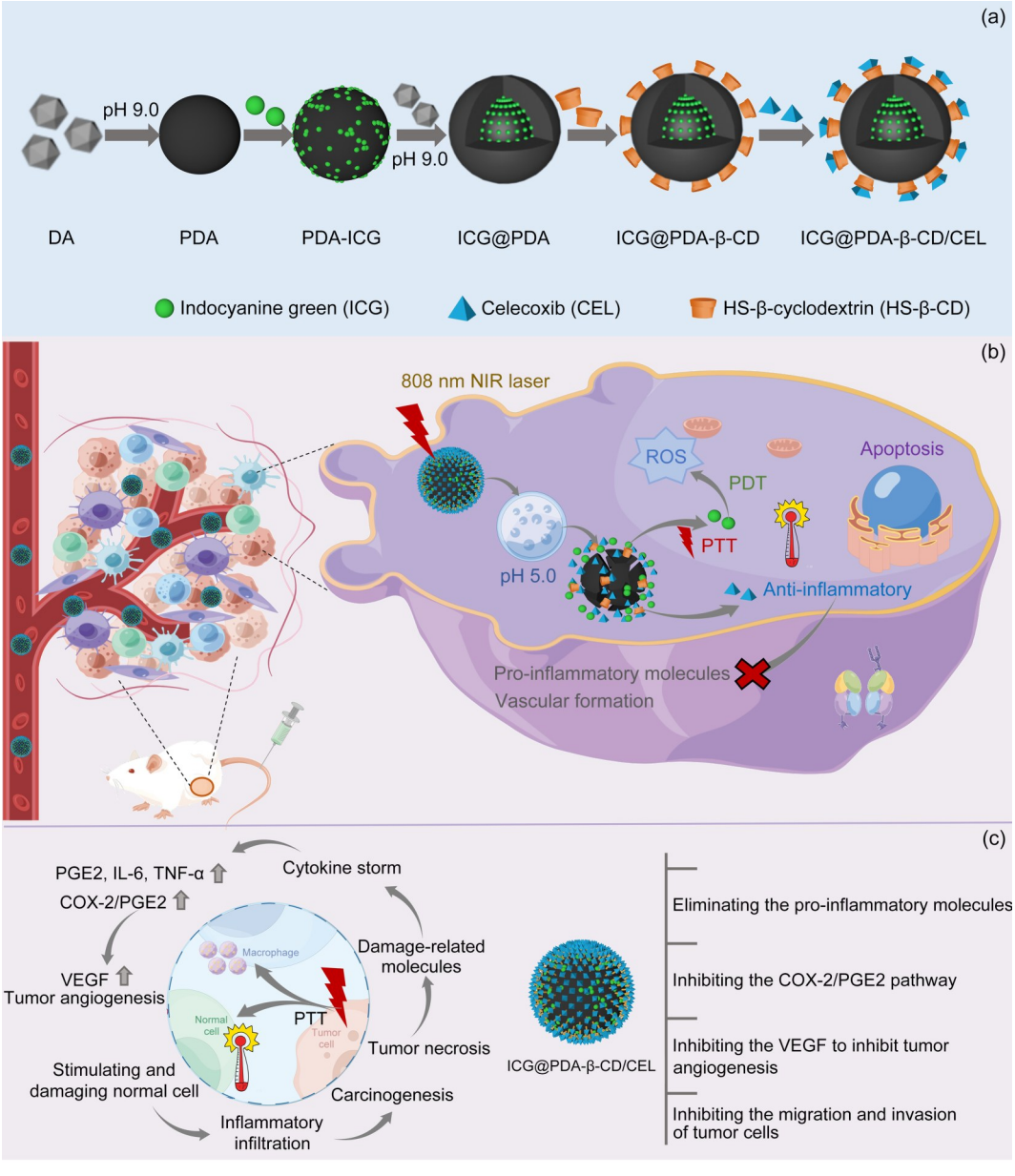

Scheme 1 Preparation and mechanism of the nanodrug delivery system ICG@PDA-β-CD/CEL for anti-inflammatory adjuvant tumor therapy. (a) Preparation of a "two-pronged" tumor nanodrug delivery system, ICG@PDA-β-CD/CEL, carrying anti-inflammatory drug CEL and the photosensitizer ICG. (b) Schematic illustration of the drug release and action mechanism of ICG@PDA-β-CD/CEL. (c) Schematic illustration of the therapeutic mechanism of ICG@PDA-β-CD/CEL in the PTT-induced inflammatory response. ROS: reactive oxygen species; PDT: photodynamic therapy

Here, W_i indicates the initial weight of ICG (or CEL), W_r denotes the weight of residual ICG (or CEL) in the supernatant (or dialysate), and W_t represents the total weight of the drug delivery system.

2.3.2 Modification of HS-β-CD on PDA

PDA contains active double bonds that chemically react with various functional groups such as amino ($–NH_2$) and sulfhydryl (–SH) [24]. To modify the PDA, HS-β-CD was added to the PDA solution and incubated for 4 h. The HS-β-CD reacted with the PDA through a Michael addition reaction, thereby forming a biparental nanocarrier, PDA-β-CD. Similarly, ICG@PDA-β-CD was obtained by adding HS-β-CD to the ICG@PDA solution.

2.3.3 Loading of CEL

CEL was loaded into the hydrophobic cavity of β-CD through hydrophilic and hydrophobic interactions. First, CEL was added to the ICG@PDA-β-CD solution, and the mixture was incubated overnight with rotation at 25 °C to

adequately accumulate CEL in the hydrophobic cavity of β-CD. To remove free CEL, the product was then successively dialyzed against 100% ethanol, 50% ethanol, and ultrapure water for 24 h (molecular weight cut-off: 14 kDa), and the final nanodrug ICG@PDA-β-CD/CEL was obtained. The mass of CEL in the dialysate was identified using high-performance liquid chromatography (HPLC), and the encapsulation rate and drug loading of CEL were calculated using Eqs. (1) and (2), respectively.

2.4 Characterization of the ICG@PDA-β-CD/CEL

The morphology and dimensions of the nanocarrier and drug delivery system were observed with a transmission electron microscope (TEM; HT-7700, Hitachi, Japan). The particle size and zeta potential were measured with a Malvern Zetasizer (Nano ZS, Malvern Instruments Ltd., UK). The ultraviolet-visible (UV–Vis) absorption spectrum was identified using a UV–Vis spectrophotometer (UV-2550, Shimadzu Ltd., Japan). HPLC analyses were conducted using an Agilent 1200 system (USA).

2.5 In vitro performance measurement

Experimental procedures S1–S4 (supplementary information) present the experimental protocol to assess the drug release, photothermal and photodynamic properties, biosafety, and protein adsorption resolution of ICG@PDA-β-CD/CEL.

2.6 Cell assays

ICG@PDA-β-CD/CEL uptake by tumor cells was determined by fluorescence colocalization imaging. To identify the cytotoxicity of ICG@PDA-β-CD/CEL, its effects on the mitochondrial membrane potential, reactive oxygen species (ROS) level, apoptosis, cloning, invasion, migration, and inflammatory factor expression in tumor cells were further determined. Experimental procedures S5–S7 (supplementary information) provide the detailed experimental protocol.

2.7 Creation of the three-dimensional (3D) tumorspheres

HeLa cells were digested and inoculated into BeyoGold^{TM} ultra-low attachment 96-well plates at a density of 5000–10000 cells per well. After 2 d, 3D tumorspheres were formed and were then treated with different formulations. Fluorescence images were captured with a confocal laser microscope (Nikon AX, Japan), with ICG serving as the indicator to assess the penetration effects of various formulations [25].

2.8 Animal assays

In vivo thermography, pharmacokinetic profile, biodistribution, tumor growth and metastasis inhibition, and ICG@PDA-β-CD/CEL biosafety were assessed by establishing U14 tumor-bearing mouse models. Inflammatory factors in the serum were detected with ELISA kits. Tumor tissues were fixed in 4% paraformaldehyde for hematoxylin and eosin (H&E), terminal deoxynucleotidyl transferase dUTP nick end labeling (TUNEL), Ki67, and immunohistochemistry staining. All experiments involving animals were conducted in accordance with the regulations of the Animal Ethics Committee of Yanshan University. Experimental procedures S8–S12 (supplementary information) show the detailed experimental protocol.

2.9 Statistical analysis

Data were presented as mean±standard deviation (SD), and statistical analysis was conducted using the default two-tailed *t*-test method in Prism (GraphPad Software Company, La Jolla, CA, USA), with significance recorded as $^{*}P<0.05$, $^{**}P<0.01$, $^{***}P<0.001$, and $^{****}P<0.0001$.

3 Results and discussion

3.1 Synthesis and characterization of ICG@PDA-β-CD/CEL

In this study, an "Oreo" nanodrug delivery system, PDA-ICG@PDA (abbreviated as ICG@PDA), was developed by coating the photosensitizer ICG onto a sandwich-like structure of PDA nanoparticles. Further, PDA-β-CD was synthesized by modifying PDA with HS-β-CD, serving as an amphiphilic carrier. The hydrophilic photosensitizer ICG was encapsulated within PDA, whereas the hydrophobic anti-inflammatory drug CEL was loaded into the hydrophobic cavity of β-CD. This resulted in the successful development of the photothermal-anti-inflammatory nanodrug delivery system ICG@PDA-β-CD/CEL, which specifically targets COX-2 (Scheme 1a).

Figures 1a–1c illustrate the morphology of the small-sized PDA core at 8 h, PDA at 12 h, and PDA-β-CD, all of which were uniformly spherical and demonstrated good dispersibility. Dynamic light scattering analysis revealed that the diameter of PDA was approximately (121.3±2.4) nm at 8 h, (210.8±3.3) nm at 12 h, and (236.7±3.7) nm for PDA-β-CD (Fig. 1d). These results indicate that DA continues to polymerize on the PDA surface to form larger PDA nanospheres and that HS-β-CD successfully modified the PDA.

Figures 1e and 1f illustrate the changes in the particle size and zeta potential after loading ICG and CEL into

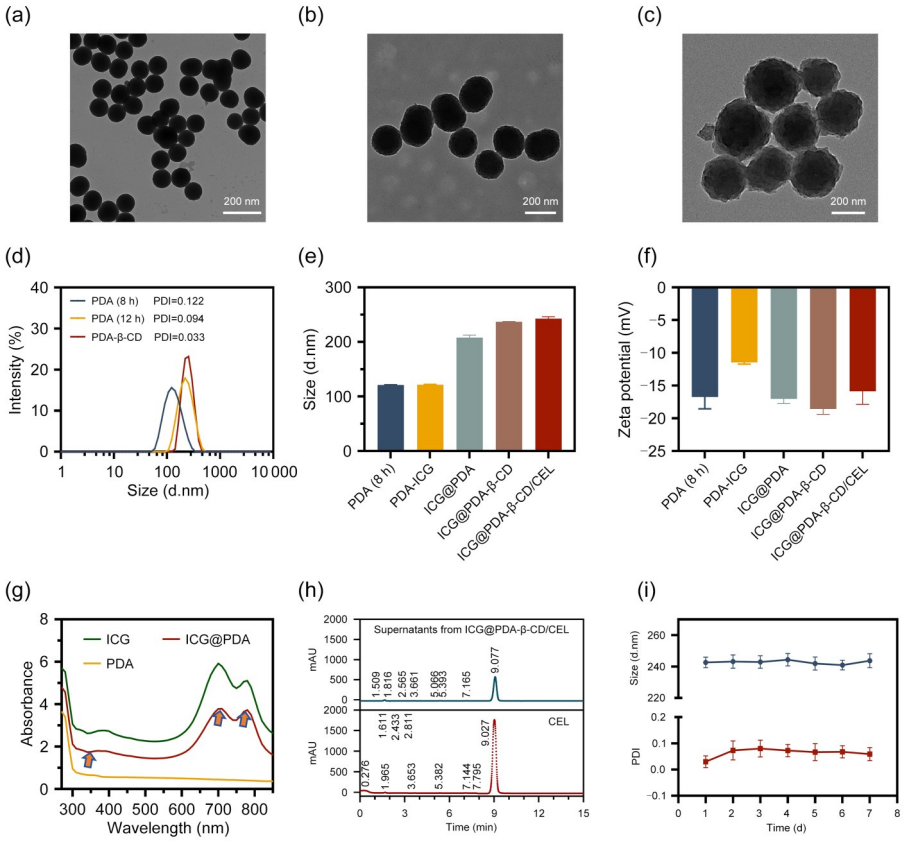

Fig. 1 Characterization of ICG@PDA-β-CD/CEL. Representative TEM images of small-sized PDA at 8 h (a), PDA at 12 h (b), and PDA-β-CD (c). (d) Hydrodynamic diameter distribution and polymer dispersity index (PDI) of PDA at 8 h, PDA at 12 h, and PDA-β-CD. Particle size (e) and zeta potential (f) of PDA at 8 h, PDA-ICG, ICG@PDA, ICG@PDA-β-CD, and ICG@PDA-β-CD/CEL. (g) UV–Vis spectrum of ICG, PDA, and ICG@PDA from 250 to 850 nm. (h) HPLC separation profiles of centrifugal supernatants from ICG@PDA-β-CD/CEL and free CEL. The HPLC separation profile with retention time of 0–8 min is magnified and presented in Fig. S1 (supplementary information). (i) Particle size and PDI changes of ICG@PDA-β-CD/CEL in 7 d. Data in (e, f, i) are expressed as mean±SD (n=3)

PDA-β-CD. Specifically, the hydrodynamic diameters for the PDA core at 8 h, PDA-ICG, ICG@PDA, ICG@PDA-β-CD, and ICG@PDA-β-CD/CEL were (121.033±0.462), (121.667±0.513), (207.933±4.366), (236.833±0.611), and (242.667±3.356) nm, with zeta potentials of (−16.733±1.815), (−11.467±0.252), (−17.033±0.702), (−18.577±0.829), and (−15.867±2.001) mV, respectively. These changes further indicate the successful synthesis of ICG@PDA-β-CD/CEL and its intermediates.

The UV–Vis absorption spectra displayed characteristic absorption peaks at 390, 710, and 780 nm for ICG in ICG@PDA-β-CD/CEL, confirming that ICG was successfully loaded into the system (Fig. 1g). The drug loading for ICG was calculated to be (8.81±1.73)%, with an encapsulation rate of (85.20±2.58)%. HPLC was used to measure CEL concentration in the supernatant after centrifuging ICG@PDA-β-CD/CEL. By comparing the HPLC results of the standard CEL solution and the supernatant, we revealed that the retention time of the CEL chromatographic peak was approximately 9 min. The peak area of the main peak (retention time: 9.077 min) in the supernatant was significantly decreased (Fig. 1h), indicating that the CEL concentration in the supernatant was significantly reduced and most of the CEL had effectively been loaded into the hydrophobic cavity of β-CD. The drug loading for CEL was (6.32±1.69)% and the encapsulation rate was (75.54±3.68)%, which were obtained using a combination of ultrafiltration and HPLC analysis. Furthermore, the particle size and polymer dispersity index (PDI) of ICG@PDA-β-CD/CEL stored in phosphate-buffered saline (PBS) (0.01 mol/L, pH: 7.4) remained stable over 7 d, indicating the formulation's ideal stability in PBS (Fig. 1i).

3.2 In vitro drug release and photothermal and photodynamic performance of ICG@PDA-β-CD/CEL

To identify whether or not the acidic conditions and temperature changes would compromise the structural integrity of ICG@PDA-β-CD/CEL, we analyzed the particle size distribution and morphology after 2 h of incubation in an acidic environment. Figures 2a–2d illustrate that the

hydrodynamic diameter of ICG@PDA-β-CD/CEL exhibited significant variability, with a noticeable heterogeneity in dispersion and signs of broken morphology. These results indicate that the complete structure of ICG@PDA-β-CD/CEL is susceptible to disruption under acidic conditions. Further, Figs. 2e and 2f demonstrated the considerably higher release rates of ICG and CEL in the acidic environment compared to PBS at a pH of 7.4. Specifically, the 12 h release rates of ICG and CEL reached 73.2% and 71.0% in acidic PBS, respectively. The release rate was further improved after infrared irradiation at 808 nm (2 W/cm^2). After irradiation, the 12 h release rates increased to 85.9% for ICG and 78.9% for CEL. The heating effect under NIR laser irradiation likely facilitated drug release from ICG@PDA-β-CD/CEL by weakening the π–π stacking interactions between ICG and PDA and accelerating nanoparticle breakdown [26].

The ICG@PDA-β-CD/CEL nanoparticles demonstrated outstanding photothermal properties caused by the unique infrared light absorption capabilities of the photosensitizer ICG and the carrier PDA. The temperature rise curves of PBS and various nanoparticle solutions under 808 nm laser irradiation were recorded, along with the photothermal images (Fig. 2g, Fig. S2 in the supplementary information). Compared to PBS, both the carrier PDA-β-CD and the photosensitizer ICG solution demonstrated significant photothermal effects, emphasizing the inherent photothermal conversion properties of PDA and ICG. Under laser irradiation, the temperature of the ICG@PDA-β-CD/CEL nanoparticle solution markedly increased, reaching 52.2 °C after 10 min, and the photothermal conversion efficiencies of PDA, ICG, ICG@PDA, and ICG@PDA-β-CD/CEL were 33.69%, 42.44%, 48.17%, and 46.08%, respectively, indicating superior photothermal properties through the synergistic integration of PDA and ICG's photothermal characteristics.

Temperatures of >43 °C reportedly induced tumor cell death; however, excessive exposure and sustained high temperatures may cause irreversible damage to surrounding healthy tissues. ICG@PDA-β-CD/CEL nanoparticles with dual photothermal properties demonstrated superior photothermal performance, which rapidly increased

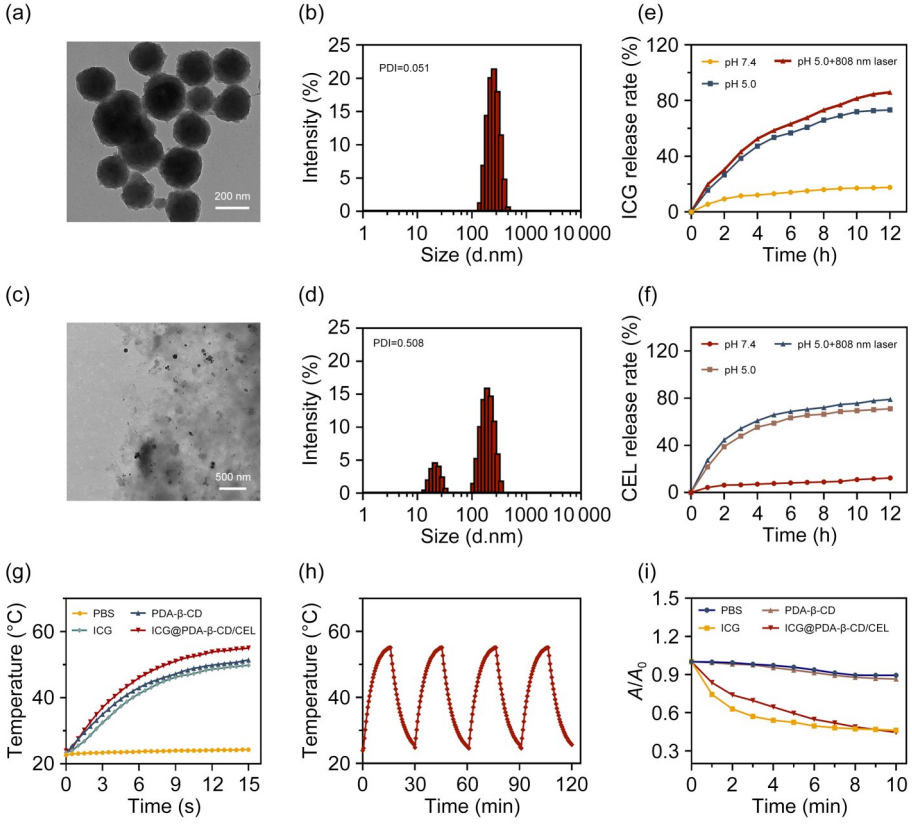

Fig. 2 Drug release profile and in vitro photothermal and photodynamic performance of ICG@PDA-β-CD/CEL. (a) Representative TEM image of ICG@PDA-β-CD/CEL. (b) Hydrodynamic diameter distribution and PDI of ICG@PDA-β-CD/CEL. (c) Representative TEM image of ICG@PDA-β-CD/CEL after acid degradation. (d) Hydrodynamic diameter distribution and PDI of ICG@PDA-β-CD/CEL after acid degradation. (e) Responsive release profile of ICG under pH of 7.4, 5.0, and 5.0 in 808 nm laser. (f) Responsive release profile of CEL under pH of 7.4, 5.0, and 5.0 in 808 nm laser. (g) Temperature elevation curves of different nanodrugs after 808 nm NIR laser irradiation (2 W/cm^2). (h) Temperature variation curve of ICG@PDA-β-CD/CEL during the NIR laser "on-off" cycle. (i) ROS production of different nanomedicines was assessed with the 1,3-diphenylisobenzofuran (DPBF) reagent (ROS capture agent)

temperatures, limiting excessive exposure and sustained high temperatures, thereby minimizing potential harm to normal tissues. Furthermore, ICG@PDA-β-CD/CEL exhibited excellent photothermal cycling performance, with stable photothermal effects after four light-cooling cycles (Fig. 2h).

ICG is the only clinically approved NIR fluorophore used in clinical applications as a photosensitizer for photodynamic therapy (PDT) [27]. The PDT performance of ICG@PDA-β-CD/CEL was assessed using the singlet oxygen indicator fluorescent probe 1,3-diphenylisobenzofuran. Figure 2i illustrates that the UV–Vis absorbance at 460 nm for ICG decreased significantly faster than that of the ICG@PDA-β-CD/CEL solution with prolonged NIR illumination. However, the final rate of decline in the UV-Vis absorbance for ICG@PDA-β-CD/CEL was nearly comparable to that of free ICG. These results confirm that ICG@PDA-β-CD/CEL is capable of generating ROS for PDT. The slower rate of ROS production by ICG@PDA-β-CD/CEL may be attributed to the delayed ICG release.

3.3 In vitro therapeutic efficacy of ICG@PDA-β-CD/CEL

The cell counting kit-8 assay results depicted in Fig. 3a indicated no significant difference in cell viability between the PDA-β-CD treatment group and the PBS control group, indicating that the carrier itself does not exhibit significant cytotoxicity. Similarly, free CEL demonstrated no significant cytotoxicity when compared with the PBS control group, indicating that anti-inflammatory drugs do not adversely affect tumor cell viability. However, ICG+laser treatment caused significant cytotoxic effects due to the photothermal and photodynamic properties of ICG, thereby markedly reducing cell viability. Compared with free ICG, the combination of photothermal and photodynamic therapies using ICG@PDA-β-CD+laser and ICG@PDA-β-CD/CEL+laser significantly curtailed tumor cell growth. Notably, the ICG@PDA-β-CD/CEL+laser treatment demonstrated a more pronounced cell growth inhibition compared with the ICG@PDA-β-CD+laser treatment. This enhanced cytotoxicity effect can be attributed to the dual photothermal actions of both ICG and PDA, the photodynamic action exerted by ICG, and the targeted effect of CEL on the COX-2/PGE2 pathway.

Figure 3b reveals that ICG@PDA-β-CD/CEL substantially inhibited tumor proliferation, an effect that intensified with increasing concentrations. This dose-dependent response indicates the potential of this formulation for effective tumor treatment.

Calcein acetoxymethyl ester/propidium iodide (Calcein/PI) co-staining of HeLa cells treated with different formulations revealed that ICG@PDA-β-CD/CEL+laser demonstrated the highest cell-killing efficiency, indicating that the combination of anti-inflammatory therapy with dual photothermal and photodynamic therapies is highly effective in eradicating tumor cells in vitro (Fig. S3 in the supplementary information). Further, a significant reduction in the mitochondrial membrane potential, a key indicator of early apoptosis, was observed in cells treated with ICG@PDA-β-CD/CEL+laser, indicating increased early apoptosis (Fig. S4 in the supplementary information). These results collectively demonstrate that ICG@PDA-β-CD/CEL combined with 808 nm laser irradiation achieves a synergistic effect, combining dual PTT, PDT, and anti-inflammatory therapy to effectively target tumor cells.

To assess the intracellular uptake of ICG@PDA-β-CD/CEL in HeLa cells, fluorescence microscopy was conducted using ICG as a tracer. Figure 3c illustrates the red fluorescence of ICG both in the cytoplasm and nucleus of the HeLa cells, which closely coincided with the blue fluorescence marking the nucleus, stained by 4',6-diamidino-2-phenylindole (DAPI). This indicates the successful loading of ICG into the ICG@PDA-β-CD/CEL nanoparticles and demonstrates that these nanoparticles are effectively endocytosed by the tumor cells, enabling them to function intracellularly.

To further investigate the photodynamic effect of ICG@PDA-β-CD/CEL, we used 2',7'-dichlorodihydrofluorescein diacetate (DCFH-DA) as a probe to measure intracellular ROS levels after treatment with various nanomaterials. Figure 3d illustrates that both the free ICG+laser treatment group and the ICG@PDA-β-CD/CEL+laser treatment group demonstrated strong green fluorescence signals, confirming that ICG@PDA-β-CD/CEL+laser generates significant ROS levels in tumor cells, exerting the efficacy of PDT. Building on the robust tumor-killing and apoptosis-inducing effects of ICG@PDA-β-CD/CEL, we hypothesized that this nanoparticle significantly inhibits tumor cell migration, invasion, and colony formation. To investigate this, we conducted scratch assays, transwell experiments, and colony formation tests. Figure 3e illustrates that, compared with the PBS treatment, the ICG@PDA-β-CD+laser treatment partially inhibited cell invasion, migration, and colony formation. Notably, ICG@PDA-β-CD/CEL+laser treatment almost completely blocked HeLa cell invasion and substantially reduced their migration and colony formation capabilities. The aforementioned research results indicate that CEL loading effectively killed tumor cells and inhibited tumor cell invasion, metastasis, and colony formation. Building on this information, we further investigated the molecular mechanisms underlying these effects. We treated HeLa cells with different formulations, harvested the cells, and analyzed their COX-2 expression levels with western blotting. Concurrently, the culture medium from the HeLa cells was collected, and PGE2, TNF-α, and IL-6

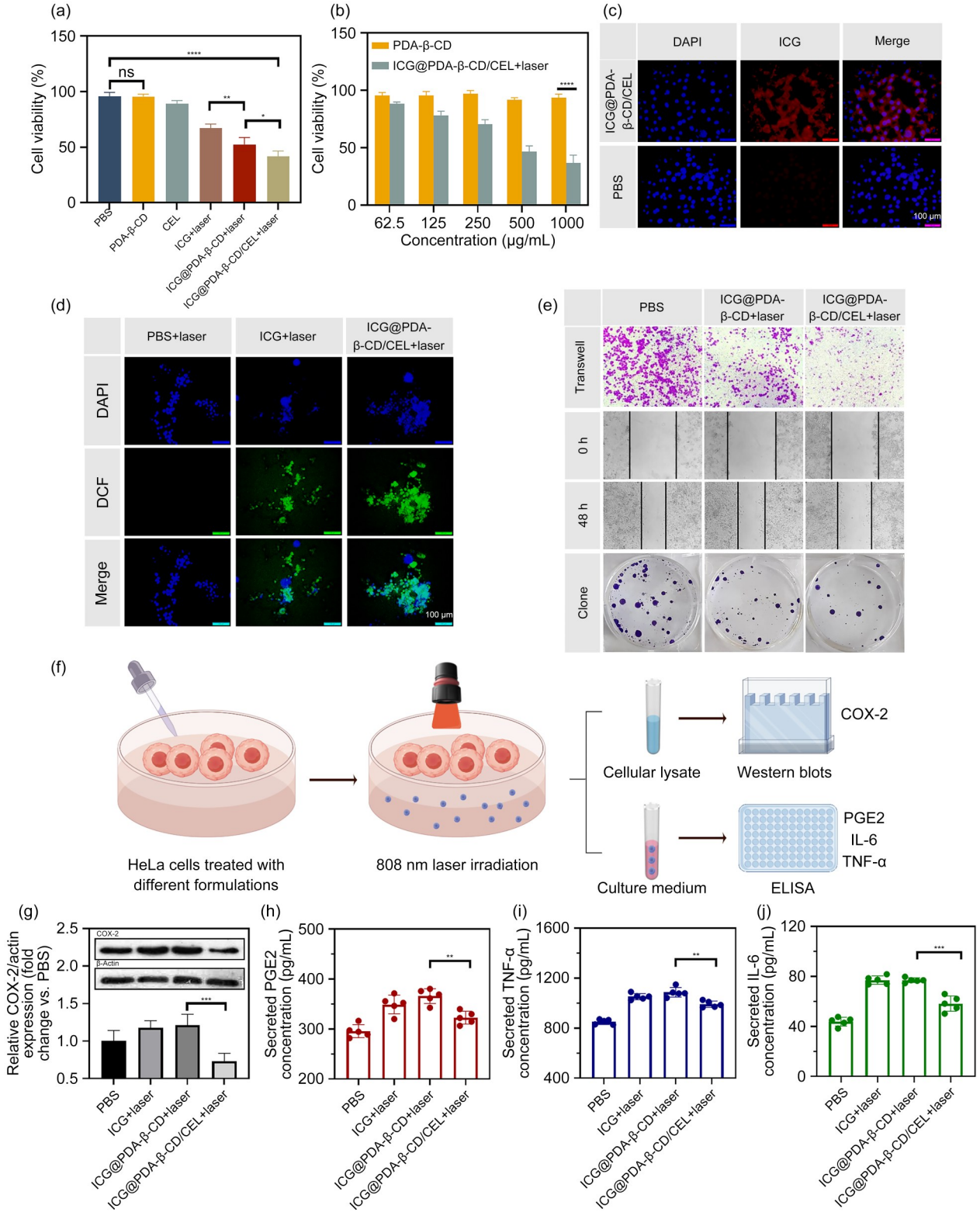

Fig. 3 In vitro therapeutic efficacy of ICG@PDA-β-CD/CEL. (a) Cytotoxicities of different nanoparticles. (b) Cytotoxicities of ICG@PDA-β-CD/CEL and PDA-β-CD at various concentrations. (c) Colocalization fluorescence images of HeLa cells treated with ICG@PDA-β-CD/CEL. (d) ROS generation of HeLa cells treated with different formulations. (e) Invasion, scratch healing, and clone formation of HeLa cells treated with different formulations. (f) Schematic diagram of COX-2 expression in tumor cells and detection of inflammation-related factors secreted by tumor cells. (g) Expression and quantification of COX-2 in HeLa cells treated with different nanoparticles. (h–j) PGE2, TNF-α, and IL-6 in the supernatant of HeLa cells treated with different nanoparticles using the ELISA method. Data in (a, b, g–j) are expressed as mean±SD (n=5). $^{*}P$<0.05, $^{**}P$<0.01, $^{***}P$<0.001, and $^{****}P$<0.0001; ns: not significant

secretion levels were quantified using the ELISA method. The experimental procedures detailed in Figs. 3f–3j illustrate that the photothermal treatment provided by ICG+laser and ICG@PDA-β-CD+laser increased COX-2 expression and heightened inflammatory factor secretion by HeLa cells compared with the PBS control group. In contrast, when loaded with the anti-inflammatory drug CEL, the ICG@PDA-β-CD/CEL+laser treatment group demonstrated reduced COX-2 expression in tumor cells (Fig. 3g) and decreased inflammatory factor secretion, including PGE2, TNF-α, and IL-6 (Figs. 3h–3j). These results indicate that CEL effectively counteracts the inflammatory response induced by PTT. Moreover, the combination of PTT with anti-inflammatory treatment suppressed the progression and metastasis of tumor cells by inhibiting the relevant inflammatory pathways.

3.4 Tumor penetration, long circulation, and tumor targeting of ICG@PDA-β-CD/CEL in vitro and in vivo

Figure 4a illustrates that the fluorescence signal of ICG in the nonilluminated ICG@PDA-β-CD/CEL group reached a 100 μm distance from the *z*-axis within 1 h. After NIR light irradiation, the temperature increase in the ICG@PDA-β-CD/CEL solution facilitated the release of ICG. This release was promoted by weakening the π–π stacking interaction between ICG and PDA, and the increased temperature

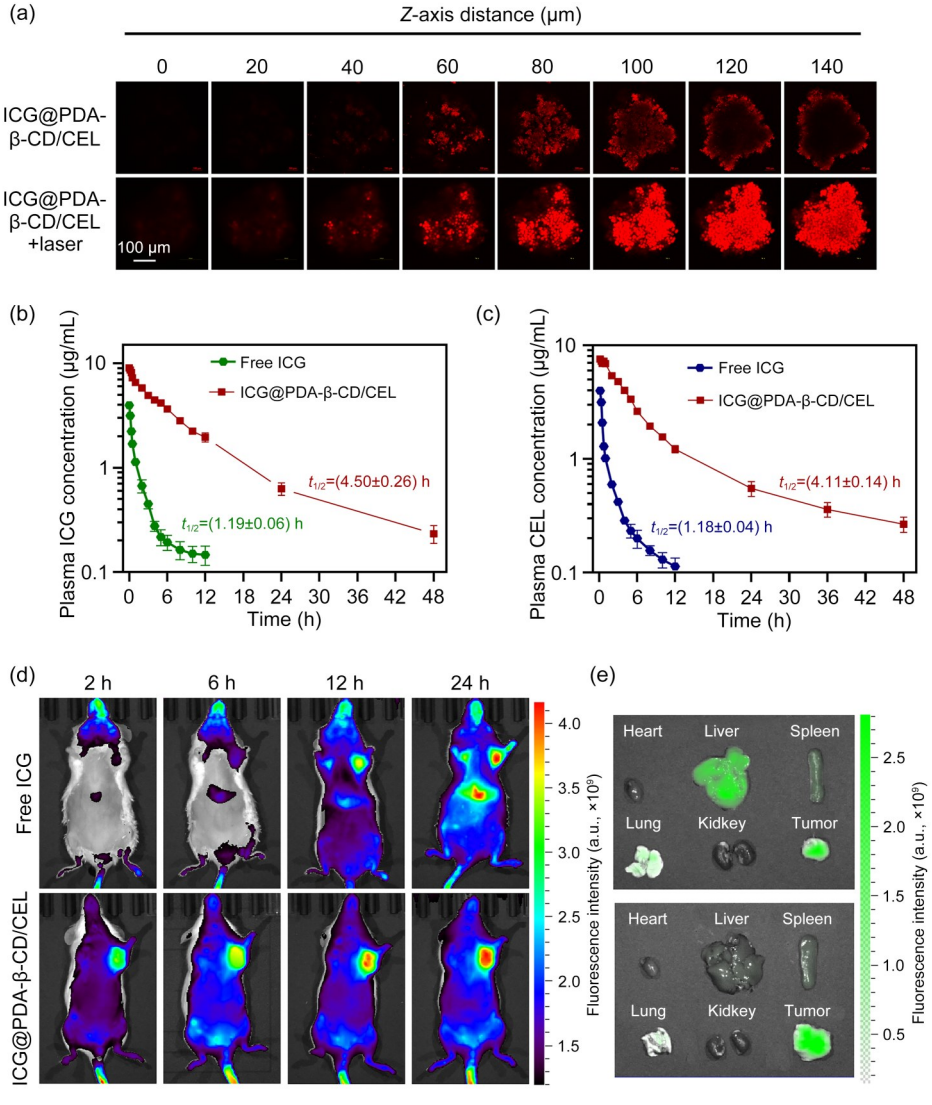

Fig. 4 Drug penetration, biodistribution, and pharmacokinetics of ICG@PDA-β-CD/CEL. (a) Laser confocal scanning images demonstrating the distribution of ICG@PDA-β-CD/CEL in the 3D tumorspheres of HeLa cells. (b, c) Plasma concentration–time profiles showing the circulation and metabolism of ICG and CEL in mice. (d) Fluorescence imaging of ICG@PDA-β-CD/CEL distribution in U14 tumor-bearing mice in vivo. (e) Ex vivo ICG fluorescence imaging of major organs and tumors excised at 24 h after the tail vein injection of ICG@PDA-β-CD/CEL. Data in (b, c) are expressed as mean±SD (n=3)

changed cellular fluidity and permeability. Consequently, these changes significantly improved the penetration and diffusion of ICG@PDA-β-CD/CEL within the tumor cell sphere, enabling the fluorescence signal of ICG to permeate the entire tumor cell sphere within 1 h.

Blood circulation plays a crucial role in tumor targeting in vivo [28]. Figures 4b and 4c demonstrate that the incorporation of the amphipathic carrier PDA-β-CD improves the pharmacokinetic profiles of ICG and CEL. When encapsulated within ICG@PDA-β-CD/CEL, both ICG and CEL demonstrated significantly prolonged blood circulation times compared with their free forms. This extended circulation facilitates greater drug accumulation at the tumor site. Once inside the tumor cells via endocytosis, the drugs can more effectively deliver combined PTT, PDT, and anti-inflammatory effects.

Figure 4d illustrates the highly specific distribution of ICG@PDA-β-CD/CEL at the mouse tumor sites, facilitated by the EPR effect. Over time, the fluorescence signal from ICG in ICG@PDA-β-CD/CEL accumulated specifically at the tumor, emphasizing its potential for targeted tumor drug delivery. Furthermore, ex vivo organ imaging demonstrated that ICG@PDA-β-CD/CEL significantly reduced ICG accumulation in the major organs of mice (Fig. 4e). This decreased organ distribution enables prolonged circulation in the body, thereby improving targeted drug delivery to the tumor site.

3.5 Antitumor efficacy of ICG@PDA-β-CD/CEL in vivo

Encouraged by the long-term circulatory and tumor-targeting capabilities of ICG@PDA-β-CD/CEL in vivo, we further investigated its photothermal performance and antitumor effects in U14 tumor-bearing mouse models. As depicted in Fig. S6 (supplementary information), U14 cells were inoculated into the left axilla of the mice. The mice were then randomly divided into three groups: PBS, free ICG, and ICG@PDA-β-CD/CEL. Once the tumors reached a volume of 1000 mm^3, the mice received different formulations via tail vein injection, followed by 808 nm laser irradiation at the tumor site, with thermal imaging conducted at various time points. The results shown in Fig. S7 (supplementary information) indicate that, compared to the PBS group, the local temperatures of the tumors in the ICG and ICG@PDA-β-CD/CEL groups significantly increased as the laser irradiation time was extended. The PBS group showed no significant change in the tumor temperature, underscoring the potent photothermal effects of ICG. Notably, the ICG@PDA-β-CD/CEL group experienced a more rapid and substantial increase in the local tumor temperature, attributed to its effective tumor targeting and prolonged circulation in vivo. After 4 min of laser irradiation, the local tumor temperature in mice treated with ICG@PDA-β-CD/CEL reached 47.7 °C, an optimal level for in vivo PTT. This temperature is expected to yield a synergistic antitumor effect, enhanced by the anti-inflammatory properties of CEL. Consequently, a laser irradiation duration of 4 min was selected for subsequent antitumor efficacy experiments.

Figure 5a illustrates the mice administered with various formulations via tail vein injection 2 d after tumor induction. After 4 h of injection, the mice were exposed to 808 nm NIR laser irradiation (2 W/cm^2 for 4 min) for PTT. The treatment was repeated every 2 d, totaling seven sessions. Tumor growth and body weight changes were continuously monitored throughout the experiment. Figures 5b–5d illustrate decreased tumor volume to 76.8% in the ICG+ laser treatment group and 69.7% in the ICG@PDA-β-CD+ laser treatment group compared with the normal saline group, indicating that the dual photothermal effects of ICG and PDA exhibited a more effective tumor ablation in vivo. The tumor volume in the ICG@PDA-β-CD/CEL+laser treatment group was reduced further to 45.9%, with significantly lower tumor growth rates and weights compared with the ICG@PDA-β-CD+laser group. This improved effect is attributed to CEL loading, which targets the COX-2/PGE2 pathway, providing a synergistic approach to combat malignancies.

We performed H&E, Ki67, and TUNEL staining on tumor tissue slices to investigate the therapeutic mechanism of ICG@PDA-β-CD/CEL. The representative histopathological images shown in Fig. 5e indicated that ICG@PDA-β-CD/CEL+laser induced a higher degree of apoptosis and necrosis in the tumor cells and inhibited malignant proliferation. These results indicate that the anti-inflammatory properties of loaded CEL effectively augment the efficacy of PTT, thereby demonstrating significant antitumor potential and clinical application prospects for ICG@PDA-β-CD/CEL.

We then delved deeper into the mechanism behind the anti-inflammatory-assisted PTT. Figures 5f–5k indicate that PTT with ICG@PDA-β-CD+laser triggers a robust inflammatory response, evidenced by the upregulated expression of COX-2, IL-6, and TNF-α in tumors and parallel increases in multiple serum markers (COX-2, PGE2, TNF-α, IL-6, and IL-10). This hyperthermia-induced inflammation subsequently stimulates VEGF production. In contrast, ICG@PDA-β-CD/CEL+laser treatment effectively suppresses this response by downregulating key mediators (VEGF, COX-2, and NF-κB) in tumors, reducing pro-inflammatory factors (COX-2, PGE2, TNF-α, and IL-6), and concurrently enhancing the anti-inflammatory cytokine IL-10.

In conclusion, CEL in ICG@PDA-β-CD/CEL modulates the pro-inflammatory response triggered by PTT and exhibits antitumor potential by suppressing the production of COX-2/PGE2-induced VEGF and related inflammatory pathways. This formulation provides a viable strategy for addressing

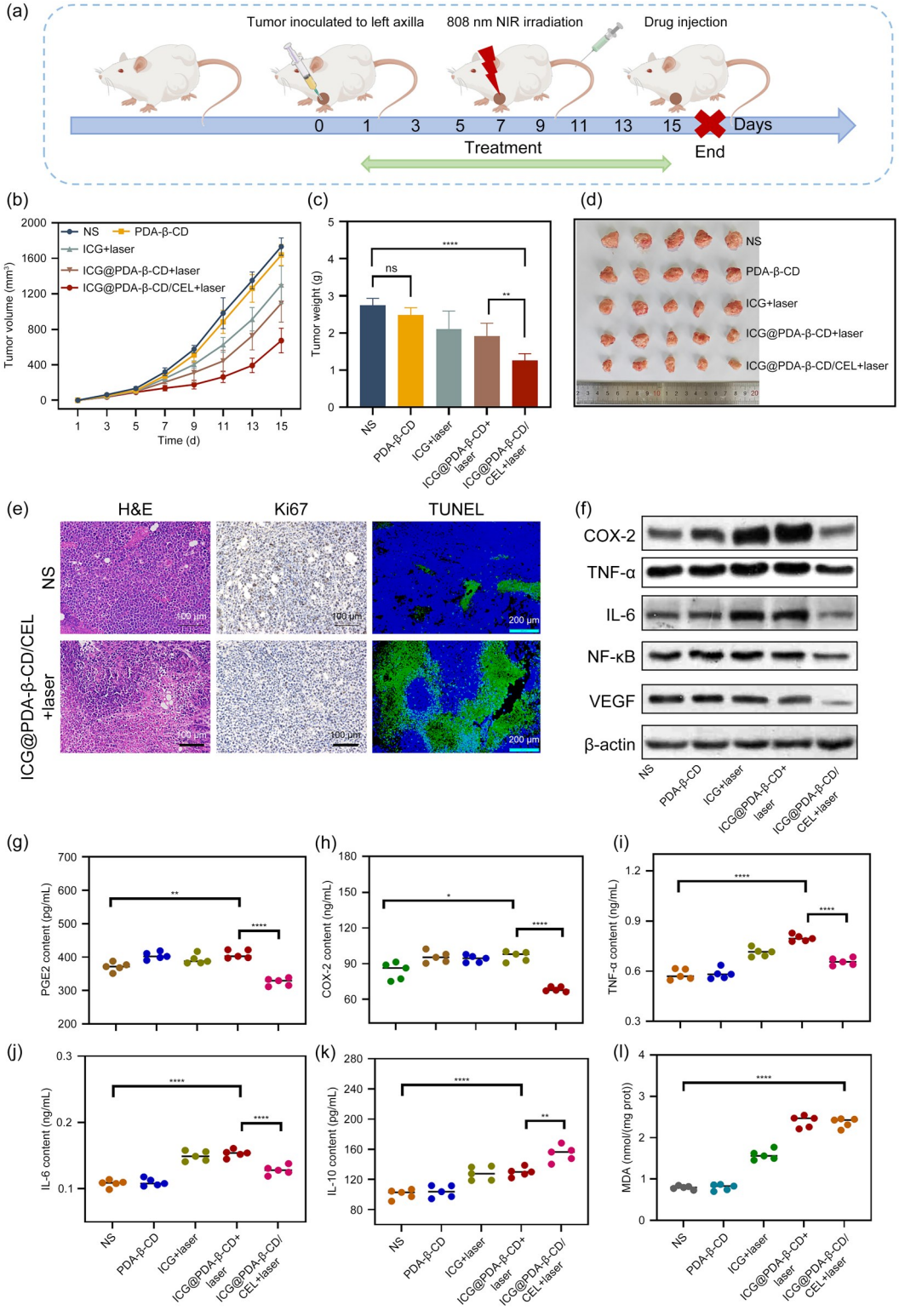

Fig. 5 Anti-inflammatory adjuvant antitumor effect of ICG@PDA-β-CD/CEL in vivo. (a) Schematic diagram of the therapeutic process in the U14 tumor-bearing mouse models. (b) Tumor volume change curves of U14 tumor-bearing mice injected with various nanodrugs. (c) Isolated tumor mass from U14 tumor-bearing mice injected with different nanodrugs. (d) Isolated tumor images from tumor-bearing mice injected with different nanodrugs. (e) Representative images of tumor tissue sections after H&E, Ki67, and TUNEL staining. (f) COX-2, TNF-α, IL-6, NF-κB, and VEGF expression in tumors from U14 tumor-bearing mice injected with different nanodrugs identified using western blot. PGE2 (g), COX-2 (h), TNF-α (i), IL-6 (j), IL-10 (k), and MDA (l) levels in the serum of U14 tumor-bearing mice injected with different nanodrugs. Data in (b, c, g–l) are expressed as mean±SD (n=5). $^{*}P$<0.05, $^{**}P$<0.01, and $^{****}P$<0.0001; ns: not significant. NS: U14 tumor-bearing mice were injected with normal saline as the control group. MDA: malondialdehyde

PTT-related complications. Further, the photodynamic treatment with ICG@PDA-β-CD/CEL+laser promotes tumor lipid peroxidation and enhances tumor cell ablation, leveraging the photodynamic capabilities conferred by the ICG loaded in ICG@PDA-β-CD/CEL (Fig. 5l).

3.6 Biosafety test of ICG@PDA-β-CD/CEL

Considering the clinical translational potential of the nano-delivery system, we further investigated the biosafety of ICG@PDA-β-CD/CEL. Figure 6a demonstrates that ICG@PDA-β-CD/CEL did not induce hemolysis, and the hemolysis rate of ICG@PDA-β-CD/CEL solutions at various concentrations was <4%, indicating its excellent biocompatibility with the blood system [21, 29, 30] and its suitability for intravenous administration. To assess the binding of ICG@PDA-β-CD/CEL to serum proteins, we developed a bovine serum albumin (BSA) adsorption model. Figure S5 (supplementary information) shows that the protein adsorption rate of gradient diluted ICG@PDA-β-CD/CEL was

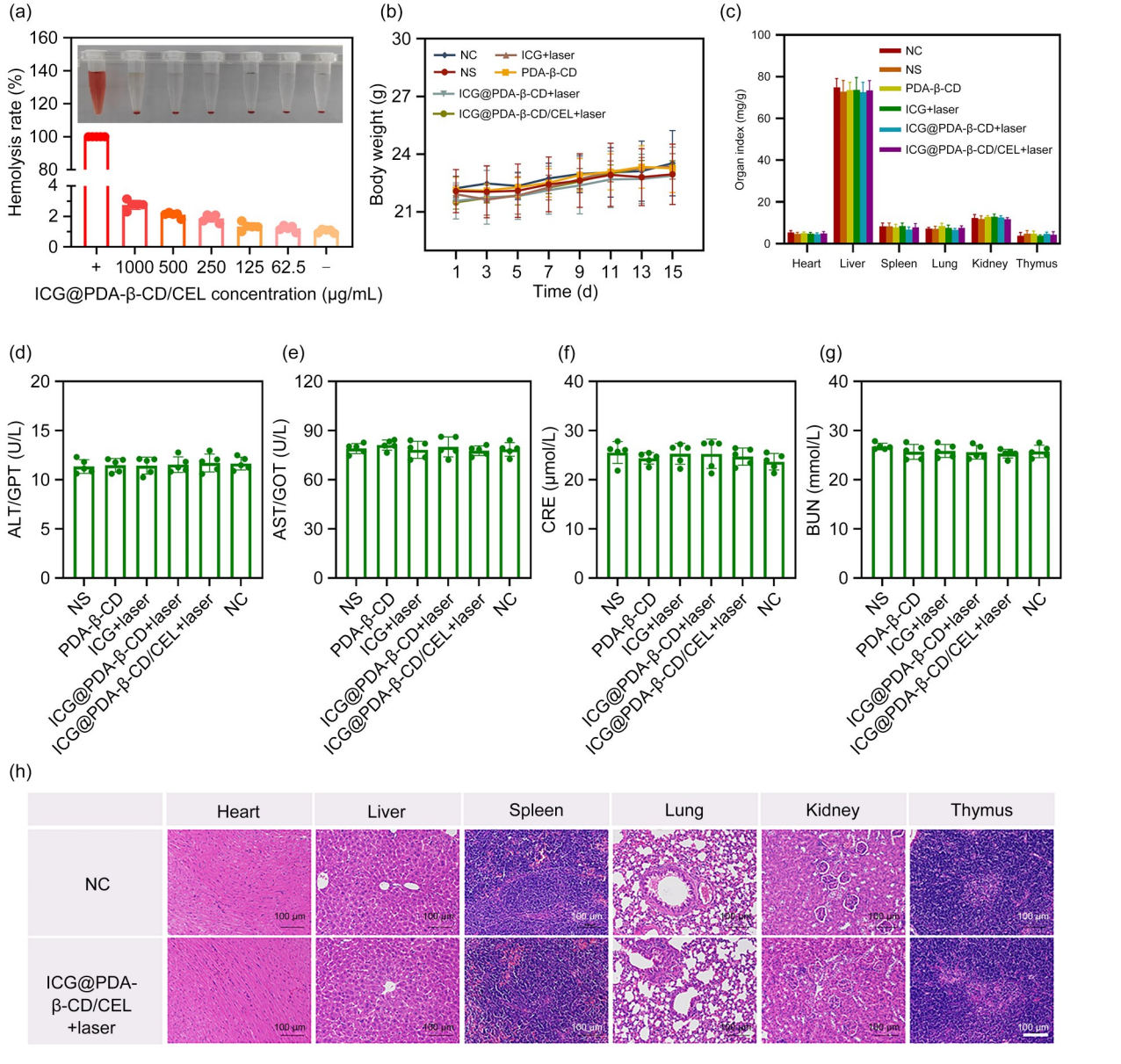

Fig. 6 Biosafety assessment of ICG@PDA-β-CD/CEL. (a) Hemolysis rate of gradient diluted ICG@PDA-β-CD/CEL in chicken erythrocytes. (b) Body weight change curves of U14 tumor-bearing mice injected with different nanodrugs. (c) Organ indices of U14 tumor-bearing mice injected with different nanodrugs. ALT (d), AST (e), CRE (f), and BUN (g) levels in the serum of U14 tumor-bearing mice injected with different nanodrugs. (h) Representative H&E images of organ tissue sections from control and ICG@PDA-β-CD/CEL-treated mice. Data in (a–g) are expressed as mean±SD (n=5). NS: U14 tumor-bearing mice were injected with normal saline as the control group; NC: normal control mice; GPT: glutamic pyruvic transaminase; GOT: glutamic oxaloacetic transaminase

all <5%, indicating that ICG@PDA-β-CD/CEL is not adsorbed by relevant serum proteins and achieves prolonged blood circulation.

Moreover, the body weights of the mice were continuously monitored throughout the experiment, and the weights of the major organs (heart, liver, spleen, lung, kidneys, and thymus) were recorded on the day of sacrifice. Figures 6b and 6c illustrate no significant changes in body weight or organ indices compared with the normal control group, with no organ enlargement or atrophy, indicating that ICG@PDA-β-CD/CEL administration did not cause significant side effects to the whole body or the major organs.

Typical hematological parameters reflecting liver and kidney function were investigated. Figures 6d–6g demonstrate no significant difference in the ALT, AST, CRE, and BUN levels between the ICG@PDA-β-CD/CEL treatment group and the normal control group or the normal saline treatment group, indicating that ICG@PDA-β-CD/CEL treatment was well tolerated without hepatorenal toxicity. Figure 6h illustrates that pathological examinations revealed no significant histological toxicity in the major organs of any group compared with the normal mouse organs. All the above results indicate that ICG@PDA-β-CD/CEL not only exhibits strong antitumor effects but also maintains good biological safety for animal organisms.

3.7 Antitumor metastasis of ICG@PDA-β-CD/CEL in vivo

The combination of PTT and anti-inflammatory therapy inhibits the development of primary tumors by targeting the related inflammatory pathways. Hence, we hypothesized that ICG@PDA-β-CD/CEL+laser plays a role in preventing the occurrence and development of metastatic tumors through fluid circulation. We developed primary-distant metastasis tumor-bearing mouse models for antitumor metastasis assessment. The treatment protocol, demonstrated in Fig. 7a, involved inoculating U14 cells in the left axilla on Day −10 as the primary tumor and in the right axilla on Day 0 as the distant metastasis tumor. Treatment concurrently commenced with the inoculation of the distant metastasis tumor and continued for 15 d, administered once every 2 d for a total of seven sessions.

Ex vivo images of the primary and distant metastasis tumors demonstrated that, compared with the ICG@PDA-β-CD treatment group, CEL loading exhibited a better therapeutic effect, with significantly reduced volumes of both primary and distant metastasis tumors (Fig. 7b). This indicates that the combination of anti-inflammatory therapy and PTT demonstrated significant inhibitory effects on both primary and metastatic tumors. The volume curves and the mass of the primary and distant tumors further confirmed the antitumor growth and metastasis effects of this combined strategy (Figs. 7c and 7d). Further, no significant difference in body weight was observed between the two mouse groups (Fig. 7e).

Immunohistochemical analysis of the tumor sections revealed that the ICG@PDA-β-CD/CEL+laser treatment significantly inhibited the positive expression of COX-2, TNF-α, and VEGF. The anti-inflammatory therapy in ICG@PDA-β-CD/CEL+laser effectively downregulated the PTT-induced inflammatory response and inhibited VEGF production, thereby preventing tumor angiogenesis.

These results indicate that CEL effectively improves PTT efficacy by inhibiting COX-2/PGE2-induced VEGF production and related inflammatory pathways. Furthermore, ICG@PDA-β-CD/CEL+laser effectively inhibited the growth of distant metastatic tumors, potentially due to the CEL-induced immune activation. We plan to further investigate the deep mechanisms of CEL as an adjuvant in tumor treatment in future experiments.

4 Conclusions

In this study, a photothermal-anti-inflammatory nanodrug delivery system, ICG@PDA-β-CD/CEL, targeting the COX-2/PGE2 pathway was developed. CEL, acting as a COX-2 inhibitor, effectively reduced inflammatory responses and specifically bound to COX-2. It was co-loaded with PDA and ICG for a combined PTT, PDT, and CEL for anti-inflammatory therapy. ICG@PDA-β-CD/CEL+laser treatment significantly inhibited tumor cell proliferation, invasion, and migration in vitro. Furthermore, the in vivo experimental results demonstrated that both the primary tumor and distant metastasis suppression rates in the ICG@PDA-β-CD/CEL+laser treatment group were significantly higher than those in the ICG@PDA-β-CD group, indicating that ICG@PDA-β-CD/CEL has substantial potential to inhibit tumor growth, migration, and metastasis. Moreover, ICG@PDA-β-CD/CEL exerted its antitumor effects by inhibiting COX-2/PGE2-induced VEGF production and associated inflammatory pathways. Meanwhile, ICG@PDA-β-CD/CEL exhibited excellent biosafety without toxic side effects. Overall, ICG@PDA-β-CD/CEL provides a viable strategy to address the challenges posed by PTT.

Supplementary Information The online version contains supplementary material available at https://doi.org/10.1631/bdm.2400470.

Acknowledgements The authors would like to greatly appreciate the Hebei Natural Science Foundation (Nos. H2023203003 and C2021203004). The flowcharting was supported by Figdraw (https://www.figdraw.com/#/. Export code: Sqexra4404, ID: AIPTI03200).

Author contributions JHC: conceptualization, methodology, and writing—original draft; ZTC: validation and formal analysis; WML: data

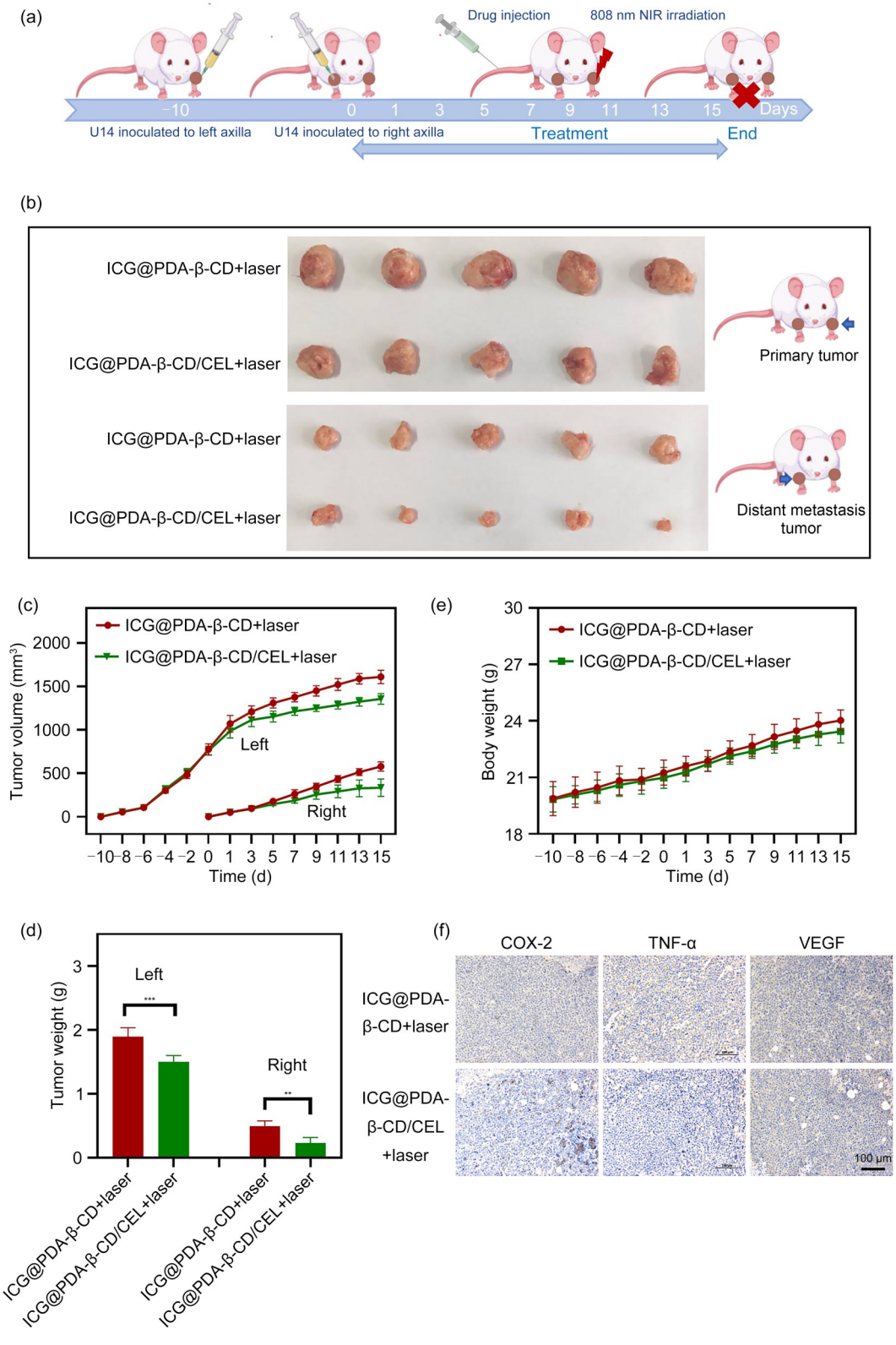

Fig. 7 ICG@PDA-β-CD/CEL inhibited tumor metastasis by exerting anti-inflammatory adjuvant effects. (a) Schematic diagram of the treatment process of the U14 bilateral tumor-bearing mouse model. (b) Isolated tumor images from tumor-bearing mice injected with different nanodrugs. (c) Volume change curves of primary and distant tumors in U14-bearing mice. (d) Weight of primary and distant tumors isolated from U14-bearing mice. (e) Body weight change curves of U14 tumor-bearing mice injected with different nanodrugs. (f) Representative COX-2, TNF-α, and VEGF immunohistochemistry images of tumor tissue sections. Data in (c–e) are expressed as mean±SD (n=5). $^{**}P<0.01$ and $^{***}P<0.001$

curation; JMS: investigation; ZHZ: investigation; SSZ: visualization; ZWL: resources; XLL: supervision and funding acquisition; JL: funding acquisition, project administration, and writing—review & editing.

Declarations

Conflict of interest The authors declare that they have no conflict of interest.

Ethical approval All animal procedures were conducted in strict compliance with the guidelines outlined in the Guide for the Care and Use of Laboratory Animals by the National Institutes of Health. The Animal Ethics Committee of Yanshan University, China, approved the study protocol (Ethics number: YD2022030).

Data availability The data that support the findings of this study are available from the corresponding author upon reasonable request.

References

1. Liao SN, Yue W, Cai SN et al (2021) Improvement of gold nanorods in photothermal therapy: recent progress and perspective. Front Pharmacol 12:664123. https://doi.org/10.3389/fphar.2021.664123
2. Zhong YL, Li TY, Zhu YF et al (2022) Targeting proinflammatory molecules using multifunctional MnO nanoparticles to inhibit breast cancer recurrence and metastasis. ACS Nano 16(12): 20430–20444. https://doi.org/10.1021/acsnano.2c06713
3. Shi CX, Dawulieti J, Shi FY et al (2022) A nanoparticulate dual scavenger for targeted therapy of inflammatory bowel disease. Sci Adv 8(4):eabj2372. https://doi.org/10.1126/sciadv.abj2372
4. Sharma A, Lee MG, Won M et al (2019) Targeting heterogeneous tumors using a multifunctional molecular prodrug. J Am Chem Soc 141(39):15611–15618. https://doi.org/10.1021/jacs.9b07171
5. Ahmadi M, Bekeschus S, Weltmann KD et al (2022) Non-steroidal anti-inflammatory drugs: recent advances in the use of synthetic COX-2 inhibitors. RSC Med Chem 13(5):471–496. https://doi.org/10.1039/d1md00280e
6. Dohadwala M, Batra RK, Luo J et al (2002) Autocrine/Paracrine prostaglandin E2 production by non-small cell lung cancer cells regulates matrix metalloproteinase-2 and CD44 in cyclooxygenase-2-dependent invasion. J Biol Chem 277(52): 50828–50833. https://doi.org/10.1074/jbc.M210707200
7. Kim HS, Sharma A, Ren WX et al (2018) COX-2 inhibition mediated anti-angiogenic activatable prodrug potentiates cancer therapy in preclinical models. Biomaterials 185:63–72. https://doi.org/10.1016/j.biomaterials.2018.09.006
8. Yang JJ, Wang X, Gao Y et al (2020) Inhibition of PI3K-AKT signaling blocks PGE_2-induced COX-2 expression in lung adenocarcinoma. OncoTargets Ther 13:8197–8208. https://doi.org/10.2147/OTT.S263977
9. Zhang Y, Zhu JY, Huang G et al (2020) Potential applications of multifunctional mesoporous carbon nanoplatform for tumor microenvironment improving by combined chemo-/phototherapy. Carbon 163:128–136. https://doi.org/10.1016/j.carbon.2020.02.029
10. Catarro M, Serrano JL, Ramos SS et al (2019) Nimesulide analogues: from anti-inflammatory to antitumor agents. Bioorg Chem 88:102966. https://doi.org/10.1016/j.bioorg.2019.102966
11. Sofia SM, Xavier CPR, Vasconcelos MH et al (2023) Repurposing some of the well-known non-steroid anti-inflammatory drugs (NSAIDs) for cancer treatment. Curr Top Med Chem 23(13):1171–1195. https://doi.org/10.2174/1568026623666230130150029
12. Cai JH, Yang YB, Zhang J et al (2024) Multilayer nanodrug delivery system with spatiotemporal drug release improves tumor microenvironment for synergistic anticancer therapy. Biofabrication 16(2):025012. https://doi.org/10.1088/1758-5090/ad22ef
13. Liu Y, Wang CN, Liu ST et al (2024) Mesoporous polydopamine nanotherapeutics for MRI-guided cancer photothermal and anti-inflammatory therapy. Int J Nanomed 19:10819–10837. https://doi.org/10.2147/IJN.S467419
14. Wang HY, Chang JJ, Pan W et al (2019) A self-assembly of an active tumor-targeted photothermal agent for enhanced anti-inflammatory cancer therapy. Nanoscale 11(39):18021–18025. https://doi.org/10.1039/C9NR06489C
15. Ren KB, Qiu Y, Yu QW et al (2021) Macrophage-mediated multi-mode drug release system for photothermal combined with anti-inflammatory therapy against postoperative recurrence of triple negative breast cancer. Int J Pharm 607:120975. https://doi.org/10.1016/j.ijpharm.2021.120975
16. Dong Q, Wang XW, Hu XX et al (2018) Simultaneous application of photothermal therapy and an anti-inflammatory prodrug using pyrene–aspirin-loaded gold nanorod graphitic nanocapsules. Angew Chem Int Ed 57(1):177–181. https://doi.org/10.1002/anie.201709648
17. Ni C, Lu JH, Chen ZA et al (2023) Preparation of polydopamine-based concave nanoparticles and mild photothermal-anti-inflammatory combination therapy for breast cancer guided by magnetic resonance imaging. Mater Des 229:111858. https://doi.org/10.1016/j.matdes.2023.111858
18. Liao T, Chen ZY, Kuang Y et al (2023) Small-size $Ti_3C_2T_x$ MXene nanosheets coated with metal-polyphenol nanodots for enhanced cancer photothermal therapy and anti-inflammation. Acta Biomater 159:312–323. https://doi.org/10.1016/j.actbio.2023.01.049
19. Jia D, Zhao S, Liu H et al (2024) ICG-labeled PD-L1-antagonistic affibody dimer for tumor imaging and enhancement of tumor photothermal-immunotherapy. Int J Biol Macromol 269:132058. https://doi.org/10.1016/j.ijbiomac.2024.132058
20. Zhang XW, Li N, Liu YP et al (2016) On-demand drug release of ICG-liposomal wedelolactone combined photothermal therapy for tumor. Nanomed Nanotechnol Biol Med 12(7): 2019–2029. https://doi.org/10.1016/j.nano.2016.05.013
21. Li J, Liu SH, Gao YT et al (2022) Layered and orthogonal assembly of hydrophilic drugs and hydrophobic photosensitizers for enhanced cancer therapy. Biomater Adv 133:112598. https://doi.org/10.1016/j.msec.2021.112598
22. Zheng XY, Chen F, Zhang JX et al (2016) Silica-assisted incorporation of polydopamine into the framework of porous nanocarriers by a facile one-pot synthesis. J Mater Chem B 4(14): 2435–2443. https://doi.org/10.1039/C5TB02784E
23. Li J, Zhang Q, Cai JH et al (2022) A double-chamber "dandelion" appearance sequential drug delivery system for synergistic treatment of malignant tumors. Int J Nanomed 17:3821–3839. https://doi.org/10.2147/ijn.s369732
24. Cho HJ, Perikamana SKM, Lee JH et al (2014) Effective immobilization of BMP-2 mediated by polydopamine coating on biodegradable nanofibers for enhanced in vivo bone formation. ACS Appl Mater Interfaces 6(14):11225–11235.

https://doi.org/10.1021/am501391z
25. Bhattacharya DS, Svechkarev D, Bapat A et al (2020) Sulfation modulates the targeting properties of hyaluronic acid to P-selectin and CD44. ACS Biomater Sci Eng 6(6):3585–3598. https://doi.org/10.1021/acsbiomaterials.0c00115
26. Tan H, Luo Z, Jia MR et al (2024) Polydopamine nanoplatform with near infrared light and pH dual stimuli-responsive for chemo-photothermal cancer therapy. Nanotechnology 35(18): 185101. https://doi.org/10.1088/1361-6528/ad22a5
27. Yang L, Huang B, Hu S et al (2022) Indocyanine green assembled free oxygen-nanobubbles towards enhanced near-infrared induced photodynamic therapy. Nano Res 15(5):4285–4293. https://doi.org/10.1007/s12274-022-4085-0
28. Lai X, Liu XL, Pan H et al (2022) Light-triggered efficient sequential drug delivery of biomimetic nanosystem for multimodal chemo-, antiangiogenic, and anti-MDSC therapy in melanoma. Adv Mater 34(10):2106682. https://doi.org/10.1002/adma.202106682
29. Li Y, Lin JY, Wang PY et al (2020) Tumor microenvironment cascade-responsive nanodrug with self-targeting activation and ROS regeneration for synergistic oxidation-chemotherapy. Nanomicro Lett 12(1):182. https://doi.org/10.1007/s40820-020-00492-4
30. Liu S, Zhang X, Bai Z et al (2024) Light/pH dual controlled drug release "nanocontainer" alleviates tumor hypoxia for synergistic enhanced chemotherapy, photodynamic therapy and chemodynamic therapy. Bio-Des Manuf 7(6):955–971. https://doi.org/10.1007/s42242-024-00310-5